Ricci Flow for 3D Shape Analysis

Wei Zeng, Dimitris Samaras, *Member*, *IEEE*, and Xianfeng David Gu, *Member*, *IEEE*

Abstract—Ricci flow is a powerful curvature flow method, which is invariant to rigid motion, scaling, isometric, and conformal deformations. We present the first application of surface Ricci flow in computer vision. Previous methods based on conformal geometry, which only handle 3D shapes with simple topology, are subsumed by the Ricci flow-based method, which handles surfaces with arbitrary topology. We present a general framework for the computation of Ricci flow, which can design any Riemannian metric by user-defined curvature. The solution to Ricci flow is unique and robust to noise. We provide implementation details for Ricci flow on discrete surfaces of either euclidean or hyperbolic background geometry. Our Ricci flow-based method can convert all 3D problems into 2D domains and offers a general framework for 3D shape analysis. We demonstrate the applicability of this intrinsic shape representation through standard shape analysis problems, such as 3D shape matching and registration, and shape indexing. Surfaces with large nonrigid anisotropic deformations can be registered using Ricci flow with constraints of feature points and curves. We show how conformal equivalence can be used to index shapes in a 3D surface shape space with the use of Teichmüller space coordinates. Experimental results are shown on 3D face data sets with large expression deformations and on dynamic heart data.

Index Terms—Ricci flow, shape representation, surface matching and registration.

✦

1 INTRODUCTION

RICCI flow is a powerful curvature flow method in Riemannian geometry. In particular, three-manifold Ricci flow has been successfully applied to recently prove the Poincaré conjecture [1]. In this work, we apply Ricci flow to 3D shape analysis. Intuitively, Ricci flow deforms the Riemannian metric of a manifold according to its curvature such that the curvature evolves according to a heat diffusion process; eventually, curvature becomes constant everywhere. The Riemannian metric with constant curvature at the steady state is called the uniformization metric. Fig. 1 illustrates the surface Ricci flow. From the left column in the figure, it is clear that any genus zero closed surface will be conformally deformed to the unit sphere $\mathbb{S}^2$. Similarly, the middle column shows that any genus one closed surface can be flattened onto the plane $\mathbb{R}^2$ periodically, where each period is a parallelogram. The right column shows that any genus two surface will be deformed onto the hyperbolic space $\mathbb{H}^2$ periodically, where each period is a hyperbolic octagon. By conformally deforming all shapes to three canonical domain ($\mathbb{S}^2, \mathbb{R}^2, \mathbb{H}^2$), all 3D shape analysis problems can be converted to 2D ones. Our first contribution in this paper is the introduction of a general framework for the computation of Ricci flow that can design Riemannian metrics by arbitrary user-defined curvatures. To ensure the generality of our framework, we generalize conventional circle packing metric to inversive distance metric (see Fig. 4)

and provide a novel convexity theorem for Ricci energy (Theorem 3.8) that can apply to all metric designs. We furthermore provide implementations of this framework for discrete surfaces with both euclidean and hyperbolic background geometries.

This work offers two more contributions by addressing two basic 3D shape analysis problems: shape indexing and deformable surface matching using Ricci flow. Shape indexing is mainly based on Teichmüller space theory, first introduced by Sharon and Mumford in their seminal work on the curve space work [2]. This work generalizes the curve shape space to 3D surface shape space. The main idea is as follows: Two surfaces are conformally equivalent if there exists an angle-preserving map between them. Fixing the topology, all of the conformal equivalence surface classes form a finite-dimensional Riemannian manifold, the so-called Teichmüller space. Each point in Teichmüller space represents a class of shapes, and the curve segment represents the deformation from one class to the other. The Riemannian metric in Teichmüller space is well defined and computable. Theoretic treatments can be found in [3]. Therefore, Teichmüller space coordinates can be used to index shapes. The Teichmüller coordinates can be explicitly computed using Ricci flow. Although this work focuses on genus zero surfaces with multiple holes, the method can be generalized to surfaces with arbitrary topologies.

The matching of 3D surfaces with large anisotropic deformation can be tackled efficiently by Ricci flow. The 3D surfaces are mapped to canonical planar domains using Ricci flow; therefore, 3D matching problems are converted to 2D matching problems. Feature constraints can be incorporated naturally to the mapping process in order to define 2D one-to-one maps that respect such constraints while still optimizing the matching energy.

Compared to existing methods, Ricci flow methods have the following merits:

Generality. None of the existing methods can handle high genus surfaces directly. For genus zero surfaces with multiple holes, none of the existing methods, such as harmonic

- *W. Zheng is with the Department of Computer Science, Wayne State University, Detroit, MI 48202. E-mail: zeng@wayne.edu.*
- *D. Samaras and X.D. Gu are with the Department of Computer Science, State University of New York at Stony Brook, Stony Brook, NY 11794. E-mail: {samaras, gu}@cs.sunysb.edu.*
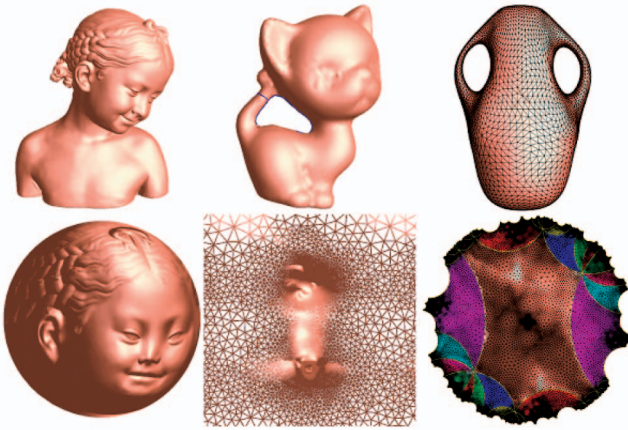
Fig. 1. Surface Uniformization Theorem: Ricci flow deforms all surfaces conformally (angle preserving) to three canonical shapes, the sphere, the plane, and the hyperbolic disk, depending on their topologies.

map [4], [5], [6], or least square conformal map (LSCM) [7], [8], can produce a one-to-one map, as demonstrated in Fig. 2. Ricci flow can handle surfaces with arbitrary topologies, and can produce one-to-one maps between surfaces with complicated topologies.

Dimension reduction. Ricci flow deforms arbitrary shapes to three canonical shapes $\mathbb{S}^2$, $\mathbb{R}^2$, and $\mathbb{H}^2$. Therefore, it converts 3D geometric problems to 2D ones. See Fig. 4.

Flexibility. In this paper, we show that previous conformal map methods [7], [9], [10], [11], [8] are subsumed by Ricci flow. The results of all existing conformal mapping methods can be achieved by the Ricci flow method, which can produce a Riemannian metric with arbitrary user-defined curvatures. In our later discussion, as examples we will concentrate all the curvature to a single feature point or several feature points using Ricci flow and make every
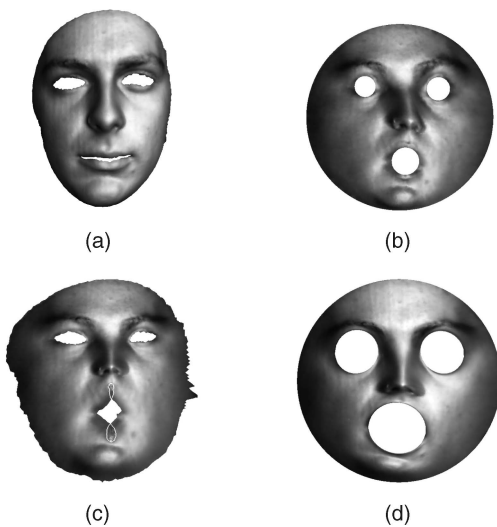

Fig. 2. Comparison of different conformal maps. Only the Ricci flow method can produce a one-to-one map for a genus zero surface with three inner holes. Neither the Least-Square Conformal Map (LSCM) method nor the Harmonic Map method can produce a one-to-one map. The LSCM result has self-intersection near the lips. The Harmonic Map result has flipped faces near the inner boundaries. (a) Multiply connected domain. (b) Ricci flow. (c) Lease-square conformal map. (d) Harmonic map.
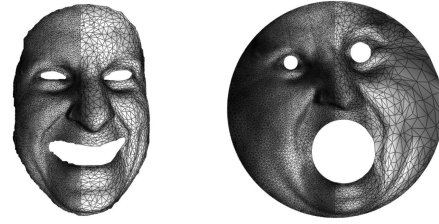

Fig. 3. Euclidean Ricci flow method is intrinsic to geometry and robust to resolution change and local noises.

other point have zero curvature. This cannot be achieved by any other method. See Fig. 10.

Discriminative power. Using Ricci flow, the intrinsic conformal geometric invariants can be computed, such as Teichmüller space coordinates, which can be used to classify surfaces accurately. None of the existing methods can compute the Teichmüller coordinates. See Figs. 13 and 14.

Invariance. Ricci flow only depends on the Riemannian metric. The results are invariant under rigid motion, scaling, and more general conformal deformations. For example, gesture change of human limbs is a conformal deformation. Running Ricci flow on the body skin surface with different gestures will produce the same result. For most elastic deformations, even when anisotropic, such as human organ deformation, their conformal images on the canonical space will be more similar than the original 3D data sets, which greatly helps for registration and matching. See Fig. 8.

Robustness. Ricci flow is intrinsic to the geometry of the surface. It is robust to triangulation of the meshes and local noises, as demonstrated in Fig. 3. While the same face surface is approximated by meshes with different resolutions, the computational results are very similar.

Rigor. The theoretic foundation for surface Ricci flow has been laid down for both smooth surfaces [12], [13] and discrete meshes [14]. This work introduces a generalized version of discrete Ricci flow; the convexity of the Ricci energy is given in Theorem 3.8.

Our experimental results demonstrate the advantages of the Ricci flow method. We show how shape indexing can be used to qualify expression changes as well as different facial geometries corresponding to different subjects. In deformable surface matching, the Ricci flow method is more accurate than existing methods [8], [6]. We show results in matching faces through different expressions as well as dynamic heart matching.

The rest of the paper is organized as follows: Previous works are reviewed briefly in Section 2. Mathematical background of the Ricci flow conformal maps is introduced in Section 3. Discrete euclidean and hyperbolic Ricci flow algorithms are explained in Section 4. Shape indexing and deformable surface matching algorithms are elaborated thoroughly in Section 5. Experimental results are reported in Section 6. Conclusions and future directions are briefly discussed in Section 7.

2   PREVIOUS WORK

In recent decades, there has been much research into surface representations for 3D shape analysis, which is fundamental for many computer vision applications, such
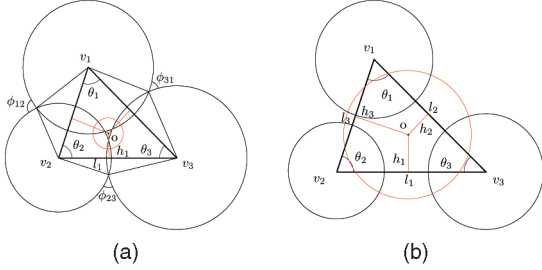
Fig. 4. Generalized circle packing metric. In this work, the circle packing metric is generalized from the conventional case to include the inversive distance metric. This greatly improves the generality and flexibility of discrete Ricci flow. (a) Conventional circle packing metric. (b) Inversive distance circle packing metric.

as 3D shape registration, partial scan alignment, 3D object recognition, and classification [15], [16], [17], [18].

In particular, as 3D scanning technologies improve, large databases of 3D scans require automated methods for matching and registration. However, matching surfaces undergoing nonrigid deformation is still a challenging problem, especially when data are noisy and with complicated topology. Different approaches include curvature-based representations [19], regional point representations [17], [20], spherical harmonic representations [21], [22], shape distributions [23], harmonic and conformal shape images [4], [8], [25], physics-based deformable models [26], Free-Form Deformation (FFD) [27], and Level-Set-based methods [28]. However, many surface representations using local shape signatures are not stable and cannot perform well in the presence of nonrigid deformation.

Elad and Kimmel [29] used isometric invariance as descriptors for 3D nonrigid shapes, such as geodesic distances. They achieved good results for expression invariant 3D face recognition in [30], where the facial expression change was modeled as near-isometries. Mémoli and Sapiro [31] proposed an isometry invariant and the Gromov-Hausdorff distance, for 3D shape comparison using point clouds. These methods handle near-isometric deformations.

Quasi-conformal deformations are more general than isometric deformations. Conformal geometric methods have been used in several applications of computer vision [4], [5], [32], [25], [2], [8], [34]. In the medical imaging field, conformal maps have been applied to brain cortex mapping. Angenent et al. [35] gave an explicit method for flattening the brain surface using certain conformal mappings from complex function theory. Gu et al. introduced a different approach for conformal brain cortex mapping using the harmonic map method [32]. Most existing conformal geometric methods can only handle genus zero surfaces.

Ricci flow can compute conformal maps for surfaces with arbitrary topologies. Surface Ricci flow was invented by Hamilton [12]. The convergence of Ricci flow on surfaces with positive Euler number is proven by Chow [13]. Discrete surface Ricci flow theory was developed by Chow and Luo [14] and a computational algorithm was introduced in [36]. Euclidean Ricci flow has been applied to shape analysis in [37]. Hyperbolic Ricci flow has been applied to 3D face matching and registration in [38]. Prior Ricci flow works were based on the conventional circle packing metric. This work generalizes the circle packing

metric to include the inversive distance metric (see Fig. 4). The theoretic results for inversive circle packing metric can be found in [39]. Furthermore, this work introduces a general framework to unify both euclidean and hyperbolic Ricci flows.

Conformal geometric methods have also been applied to the 2D shape space problem. Sharon and Mumford pioneered the curve space using the conformal welding method in [2] based on Teichmüller theory. The space of curves was modeled as an infinite-dimensional Riemannian manifold and endowed with a distance structure, which was used to measure the similarity of two curves. Later, curve space was extended in Michor and Mumford [40], Yezzi and Mennucci [41], Mio et al. [42], and Charpiat et al. [43]. This work applies Teichmuller theory to generalize curve space to 3D shape space.

3 THEORETICAL BACKGROUND

This section briefly introduces the theoretic background of Teichmüller space theory and surface Ricci flow. We refer readers to a classical text book [3] for Teichmüller theory and the seminal papers on surface Ricci flow [12], [13].

3.1 Riemannian Metric and Curvature

Definition 3.1 (Riemannian metric). *Suppose S is a surface, the Riemannian metric is a tensor $\mathbf{g} = (g_{ij})$ which is positive definite and defines an inner product for the tangent spaces of S.*

Suppose (x, y) are local coordinates of S, two tangent vectors $v_1 = (dx_1, dy_1)$, $v_2 = (dx_2, dy_2)$ are on the tangent plane at a point $p \in S$, then their inner product is defined as

$$<\mathbf{v}_1, \mathbf{v}_2>_{\mathbf{g}} = \sum_{ij} g_{ij} dx_i dy_j.$$

The angle between $\mathbf{v}_1, \mathbf{v}_2$ measured by $\mathbf{g}$ is given by

$$\theta_{\mathbf{g}} = cos^{-1} \frac{<\mathbf{v}_1, \mathbf{v}_2>_{\mathbf{g}}}{\sqrt{<\mathbf{v}_1, \mathbf{v}_1>_{\mathbf{g}} <\mathbf{v}_2, \mathbf{v}_2>_{\mathbf{g}}}}. \tag{1}$$

Definition 3.2 (Conformal Riemannian metric). *Two Riemannian metrics on S are* conformal *if there is a function defined on the surface $u : S \to \mathbb{R}$ such that $\bar{\mathbf{g}} = e^{2u}\mathbf{g}$, where u is called the* conformal factor.

Using (1), we can show that, for all angles between two tangent vectors, $\theta_{\mathbf{g}} = \theta_{\bar{\mathbf{g}}}$.

If surface metric $\mathbf{g}$ is conformal to the euclidean metric $dx^2 + dy^2$, then they are called *isothermal coordinates*: $\mathbf{g} = e^{2u(x,y)}(dx^2 + dy^2)$.

Definition 3.3 (Gaussian curvature). *Let S be a surface with a Riemannian metric $\mathbf{g}$ and (x, y) be isothermal coordinates of S, then the Gaussian curvature is defined as $k(x, y) = \Delta_{\mathbf{g}} u(x, y)$, where $\Delta_{\mathbf{g}}$ is the Laplace-Beltrami operator induced by the original metric $\mathbf{g}$ [44], $\Delta_{\mathbf{g}} = \frac{1}{e^{2u(x,y)}}(\frac{\partial^2}{\partial x^2} + \frac{\partial^2}{\partial y^2})$.*

Conformal metric deformation will change the curvatures accordingly. When the metric of S is changed from $\mathbf{g}$ to $\bar{\mathbf{g}} = e^{2u}\mathbf{g}$, then the Gaussian curvature k of interior points changes by $\bar{k} = e^{-2u}(k - \Delta_{\mathbf{g}}u)$. The geodesic curvature k_g on

the boundary points changes as $\bar{k}_g = e^{-u}(k_g - \frac{\partial u}{\partial \mathbf{n}})$, where $\mathbf{n}$ is the normal to the boundary of the surface ∂S.

Curvature is determined by the Riemannian metric and different metrics induce different curvatures. But, the total curvature is solely determined by the topology.

Theorem 3.1 (Gauss-Bonnet). *Let $(S, \mathbf{g})$ be a metric surface, the total curvature is $\int_S K dA_{\mathbf{g}} + \int_{\partial S} k_g ds = 2\pi\chi(S)$, where $\chi(S)$ is the Euler number of the surface.*

A direct corollary of Gauss-Bonnet theorem is:

Corollary 3.2 (Uniqueness of geodesic). *Let $(S, \mathbf{g})$ be a metric surface such that $\mathbf{g}$ induces nonpositive Gaussian curvature and p, q are two points on S (p may be identical to q), then there exists a unique geodesic connecting p and q in each homotopy class.*

In each conformal metric class, there is a unique metric that produces constant curvature.

Theorem 3.3 (Uniformization). *Let $(S, \mathbf{g})$ be a closed metric surface, then there exists a Riemannian metric $\bar{\mathbf{g}}$, which induces a constant Gaussian curvature, according to $\chi(S) < 0, \chi(S) = 0$ and $\chi(S) > 0$, the constant is $-1, 0, +1$, respectively.*

Fig. 1 illustrates the uniformization theorem. Uniformization metric can be computed using Ricci flow method.

3.2 Surface Ricci Flow

Ricci flow is a powerful curvature flow method, invented by Hamilton [12] for the proof of the Poincaré conjecture [46], [47], [1]. Intuitively, it describes the process to deform the Riemannian metric according to curvature such that the curvature evolves like a heat diffusion process:

$$\frac{d\mathbf{g}}{dt} = -2k\mathbf{g}. \qquad (2)$$

Hamilton [12] and Chow [13] proved the convergence of surface Ricci flow.

Theorem 3.4 (Surface Ricci flow). *For a closed surface, if the total area of the surface is preserved during the flow, the Ricci flow will converge to a metric such that the Gaussian curvature is constant everywhere.*

In our work, we compute the euclidean and hyperbolic uniformization metric using the surface Ricci flow method.

3.3 Hyperbolic Geometry

In our computational algorithms, we require the basic knowledge of hyperbolic geometry. Here, we briefly introduce the elementary concepts in hyperbolic geometry.

The hyperbolic space $\mathbb{H}^2$ cannot be realized in $\mathbb{R}^3$, instead we use the following Poincaré model to represent it.

Definition 3.4 (Poincaré disk). *The Poincaré disk is the unit disk on the complex plane $|z| < 1$, $z = x + iy$, with Riemannian metric $ds^2 = \frac{4dzd\bar{z}}{(1-\bar{z}z)^2}$.*

The *rigid motion* in the hyperbolic space is a Möbius transformation $z \to e^{i\theta}\frac{z-z_0}{1-\bar{z}_0 z}$. A *hyperbolic line* (a geodesic) is a circular arc which is orthogonal to the unit circle $|z| = 1$. A *hyperbolic circle* (c, r) (where c is the center and r is the

radius) looks like a euclidean circle (C, R), where $C = \frac{2-2\mu^2}{1-\mu^2|c|^2}$, and $R^2 = |C|^2 - \frac{|c|^2-\mu^2}{1-\mu^2|c|^2}$, where $\mu = \frac{e^r-1}{e^r+1}$.

There are other models of hyperbolic space. Another commonly used one is the *Klein model* [48]. The Klein model is also the unit disk, where all geodesics are straight euclidean lines. This fact greatly simplifies the computation in practice. The conversion from the Poincaré disk to the Klein model is straightforward:

$$z \to \frac{2z}{1+\bar{z}z}. \qquad (3)$$

The Poincaré model is conformal, whereas the Klein model is not. In our work, we compute the shortest path connecting two hyperbolic lines. The following lemma ensures the uniqueness of such kind of curve:

Lemma 3.5 (Shortest path). *Given two hyperbolic lines γ_1, γ_2 at the general position, there exists a unique hyperbolic line γ_3 orthogonal to both of them. γ_3 is the shortest path between γ_1 and γ_2.*

The proof is straightforward. Using the Poincaré disk model, from the euclidean geometry point of view, γ_3 is a geodesic, which is a euclidean circle orthogonal to three circles: the unit circle, the circle including γ_1, and the circle including γ_2. Such a circle exists and is unique.

3.4 Discrete Theory

In computer vision, surfaces are approximated by piecewise linear triangular meshes. In this section, smooth surface Ricci flow is generalized to the discrete setting.

Suppose $M(V, E, F)$ is a simplicial complex (triangle mesh) with vertex set V, edge set E, and face set F, respectively. We use v_i to denote the ith vertex, $[v_i, v_j]$ the edge connecting v_i and v_j, and $[v_i, v_j, v_k]$ the face formed by v_i, v_j, v_k.

Definition 3.5 (Discrete metric). *A discrete metric on M is a function $l : E \to \mathbb{R}^+$ such that, on each face $[v_i, v_j, v_k]$, the triangle inequality holds $l_{ij} + l_{jk} > l_{ki}$.*

Given a discrete metric, each face on the mesh can be treated as a triangle embedded in different spaces. This defines the background geometry.

Definition 3.6 (Background geometry). *Let M be a 2D simplicial complex, with a discrete metric. If each face of M is a euclidean triangle, then the mesh is with euclidean $\mathbb{E}^2$ background geometry. If each face is a hyperbolic triangle, then the mesh is with hyperbolic $\mathbb{H}^2$ background geometry.*

The discrete metric determines the corner angles on each face by the cosine law,

$$\theta_i = \begin{cases} \cos^{-1}\frac{l_j^2+l_k^2-l_i^2}{2l_jl_k}, & \mathbb{E}^2, \\ \cos^{-1}\frac{\cosh l_j \cosh l_k - \cosh l_i}{2\sinh l_j \sinh l_k}, & \mathbb{H}^2. \end{cases} \qquad (4)$$

The discrete Gaussian curvature is defined as angle deficient.

Definition 3.7 (Discrete Gaussian curvature). *Suppose M is a mesh with a discrete metric, which either in euclidean or hyperbolic background geometry. $[v_i, v_j, v_k]$ is a face in M*

and θ_i^{jk} represents the corner angle at v_i on the face. The discrete Gaussian curvature of v_i is defined as

$$K_i = \begin{cases} 2\pi - \sum_{jk} \theta_i^{jk}, & v_i \notin \partial M, \\ \pi - \sum_{jk} \theta_i^{jk}, & v_i \in \partial M. \end{cases} \tag{5}$$

The total Gaussian curvature is controlled by the topology of the mesh:

$$\sum_i K_i + \lambda \sum_{ijk} A_{ijk} = 2\pi\chi(M), \tag{6}$$

where A_{ijk} is the area of the face $[v_i, v_j, v_k]$, λ is zero if M is with euclidean background metric, -1 if M is with hyperbolic background metric.

3.5 Generalized Discrete Ricci Flow

The discrete Ricci flow method used in this work generalizes the conventional discrete Ricci flow [14], [37]. The conventional discrete Ricci flow can only handle the cases, as shown in Fig. 4a. The inversive distance metric is introduced to generalize the discrete Ricci flow, which handles both cases in the figure. This improves generality and flexibility of the discrete Ricci flow method.

A *circle packing* associates each vertex with a circle. The circle at vertex v_i is denoted as c_i. The two circles c_i and c_j on an edge $[v_i, v_j]$ are disjoint, as shown in Fig. 4b, or intersect each other at acute angle $\theta_{ij} < \frac{\pi}{2}$, as shown in the left frame.

Definition 3.8 (Inversive distance). *Suppose the length of $[v_i, v_j]$ is l_{ij}, the radii of c_i and c_j are γ_i and γ_j, respectively, then the inversive distance between c_i and c_j is given by*

$$I(c_i, c_j) = \begin{cases} \frac{l_{ij}^2 - \gamma_i^2 - \gamma_j^2}{2\gamma_i \gamma_j}, & \mathbb{E}^2, \\ \frac{\cosh l_{ij} - \cosh \gamma_i \cosh \gamma_j}{\sinh \gamma_i \sinh \gamma_j}, & \mathbb{H}^2. \end{cases} \tag{7}$$

The generalized circle packing metric is defined as

Definition 3.9 (Generalized circle packing metric). *A generalized circle packing metric on a mesh M is to associate each vertex v_i with a circle c_i, whose radius is γ_i, associate each edge $[v_i, v_j]$ with a nonnegative number I_{ij}. The edge length is given by*

$$l_{ij} = \begin{cases} \sqrt{\gamma_i^2 + \gamma_j^2 + 2I_{ij}\gamma_i \gamma_j}, & \mathbb{E}^2, \\ \cosh^{-1}(\cosh \gamma_i \cosh \gamma_j + I_{ij} \sinh \gamma_i \sinh \gamma_j), & \mathbb{H}^2. \end{cases} \tag{8}$$

The circle packing metric is denoted as (Γ, I, M), where $\Gamma = \{\gamma_i\}$, $I = \{I_{ij}\}$.

A *discrete conformal deformation* is to change radii γ_is only, and preserve inverse distance I_{ij}s. The discrete Ricci flow is defined as follows: Let

$$u_i = \begin{cases} \log \gamma_i, & \mathbb{E}^2, \\ \log \tanh \frac{\gamma_i}{2}, & \mathbb{H}^2. \end{cases}$$

Definition 3.10 (Discrete Ricci flow). *Given a circle packing metric (Γ, I, M), the discrete Ricci flow is*

$$\frac{du_i}{dt} = \bar{K}_i - K_i, \tag{9}$$

where $\bar{K}_i$ is the user-defined curvature at vertex v_i.

Given a triangle $[v_i, v_j, v_k]$ with a circle packing, there exists a unique circle c, which is orthogonal to c_i, c_j, c_k, shown as the red circles in Fig. 4. The center of c is O. The distance from O to edge $[v_i, v_j]$ is denoted as h_k, and the edge length of $[v_i, v_j]$ is denoted as l_k.

Lemma 3.6. *The following symmetric relation holds for euclidean Ricci flow:*

$$\frac{\partial \theta_i}{\partial u_j} = \frac{\partial \theta_j}{\partial u_i} = \frac{h_k}{l_k} \tag{10}$$

and

$$\frac{\partial \theta_i}{\partial u_i} = -\frac{\partial \theta_i}{\partial u_j} - \frac{\partial \theta_i}{\partial u_k}. \tag{11}$$

For the hyperbolic Ricci flow, similar symmetry holds, albeit with a more complex formula. On one face $[v_1, v_2, v_3]$,

$$\begin{pmatrix} d\theta_1 \\ d\theta_2 \\ d\theta_3 \end{pmatrix} = \frac{-1}{\sin\theta_1 \sinh l_2 \sinh l_3} M \begin{pmatrix} du_1 \\ du_2 \\ du_3 \end{pmatrix}, \tag{12}$$

$$M = \begin{pmatrix} 1 - a^2 & ab - c & ca - b \\ ab - c & 1 - b^2 & bc - a \\ ca - b & bc - a & 1 - c^2 \end{pmatrix} \Lambda \begin{pmatrix} 0 & ay - z & az - y \\ bx - z & 0 & bz - x \\ cx - y & cy - x & 0 \end{pmatrix},$$

$$\Lambda = \begin{pmatrix} \frac{1}{a^2 - 1} & 0 & 0 \\ 0 & \frac{1}{b^2 - 1} & 0 \\ 0 & 0 & \frac{1}{c^2 - 1} \end{pmatrix},$$

where

$$(a, b, c) = (\cosh l_1, \cosh l_2, \cosh l_3)$$

and

$$(x, y, z) = (\cosh \gamma_1, \cosh \gamma_2, \cosh \gamma_3).$$

Lemma 3.7. *The following symmetric relation holds for hyperbolic Ricci flow:*

$$\frac{\partial \theta_i}{\partial u_j} = \frac{\partial \theta_j}{\partial u_i}.$$

Let **u** represent the vector $(u_1, u_2, \ldots u_n)$ and **K** represent the vector $(K_1, K_2, \ldots, K_n)$. where $n = |V|$. Fixing the inversive distances, all possible **u**s that ensure the triangle inequality on each face form the *admissible metric space* of M, which is a simply connected domain in R^n. The above lemma proves that the differential one-form $\omega = \sum_i (\bar{K}_i - K_i)du_i$ is a closed one-form. The discrete euclidean Ricci energy and hyperbolic Ricci energy have the same formula.

Definition 3.11 (Discrete Ricci energy). *The discrete euclidean and Hyperbolic Ricci energy is defined as*

$$E(\mathbf{u}) = \int_{\mathbf{u_0}}^{\mathbf{u}} \sum_i (\bar{K}_i - K_i) du_i,$$

where $\mathbf{u_0} = (0, 0, \ldots, 0)$.

The discrete Ricci flow in (9) is the negative gradient flow of the Ricci energy. The following convexity theorem lays down the theoretic foundation of our algorithm:

Theorem 3.8 (Convexity of Ricci energy). *The discrete euclidean Ricci energy is convex on the hyperplane $\sum_i u_i = 0$ in the admissible metric space. The discrete hyperbolic Ricci energy is convex in the admissible metric space.*

Detailed proof for the conventional circle packing metric can be found in [14] and for the inversive distance circle packing metric can be found in [39]. The metric inducing the target curvature is the unique global optimum of the Ricci energy. Therefore, the discrete Ricci flow will not get stuck at any local optimum, and converges to the global optimum.

4 ALGORITHMS

This section provides the implementation details for generalized discrete Ricci flow on triangular meshes with euclidean and hyperbolic background geometries. In the following discussion, we simply call them euclidean and hyperbolic Ricci flow.

4.1 Generalized Circle Packing Metric

Algorithm 1 computes the initial generalized circle packing metric on meshes for both euclidean and hyperbolic Ricci flow.

Algorithm 1. Initial Circle Packing Metric
Require: A triangular mesh M, embedded in $\mathbb{R}^3$.
1: **for all** face $[v_i, v_j, v_k] \in M$ **do**

2:     Compute $\gamma_i^{jk} = \frac{l_{ij} + l_{ki} - l_{jk}}{2}$.
3: **end for**
4: **for all** vertex $v_i \in M$ **do**
5:     Compute the radius $\gamma_i = \min_{jk} \gamma_i^{jk}$.
6: **end for**
7: **for all** edge $[v_i, v_j] \in M$ **do**
8:     Compute the inversive distance using (7).
9: **end for**

4.2 Discrete Ricci Flow

The discrete euclidean and Hyperbolic Ricci flow algorithm is explained in Algorithm 2, which produces a metric, inducing user-defined target curvature $\bar{K}$.

Algorithm 2. Generalized Euclidean and; Hyperbolic Ricci Flow
Require: A triangular mesh M, the target curvature $\bar{K}$.
1: Compute the initial circle packing metric using Algorithm 1.
2: **repeat**
3:     For each edge, compute the edge length using (8)
4:     For each face $[v_i, v_j, v_k]$, compute the corner angles θ_i, θ_j and θ_k, using $\mathbb{E}^2$ or $\mathbb{H}^2$ cosine laws (4).

5:     For each face $[v_i, v_j, v_k]$, compute $\frac{\partial \theta_i}{\partial u_j}, \frac{\partial \theta_j}{\partial u_k}$, and $\frac{\partial \theta_k}{\partial u_i}$ using (10) for $\mathbb{E}^2$ case and (12) for $\mathbb{H}^2$ case.
6:     For each face $[v_i, v_j, v_k]$, compute $\frac{\partial \theta_i}{\partial u_i}, \frac{\partial \theta_j}{\partial u_j}$ and $\frac{\partial \theta_k}{\partial u_k}$ using (11) for $\mathbb{E}^2$ case, and (12) for $\mathbb{H}^2$ case.
7:     Construct the Hessian matrix H.
8:     Solve linear system $H\delta\mathbf{u} = \bar{K} - K$.
9:     Update discrete conformal factor $\mathbf{u} \leftarrow \mathbf{u} + \delta\mathbf{u}$.
10:     For each vertex v_i, compute the Gaussian curvature K_i.
11: **until** $\max_{v_i \in M} |\bar{K}_i - K_i| < \epsilon$

4.3 Embedding

After computing the discrete metric of the mesh, we can embed the mesh onto $\mathbb{R}^2$ or $\mathbb{H}^2$. As described in Algorithm 3, basically, we isometrically flatten triangle by triangle using the euclidean or hyperbolic cosine law.

Algorithm 3. Embedding
Require: A triangular mesh M, a set of fundamental group generators intersecting only at the base point p, using the algorithm in [49].
1: Slice M along the fundamental group generators to form a fundamental domain $\bar{M}$.
2: Embed the first triangle $[v_0, v_1, v_2] \in \bar{M}$, map each v_i to $\tau(v_i)$ on the complex plane $\mathbb{C}$. $(\tau(v_0), \tau(v_1), \tau(v_2))$ are
$$\mathbb{R}^2 : (0, l_{01}, l_{20} e^{i\theta_0^{12}})$$

$$\mathbb{H}^2 : (0, \tanh \frac{l_{01}}{2}, \tanh \frac{l_{02}}{2} e^{i\theta_0^{12}}).$$
3: Put all the neighboring faces of the first face to a face queue.
4: **while** the face queue is not empty **do**
5:     Pop the first face $[v_i, v_j, v_k]$ from the queue.
6:     Suppose v_i and v_j has been embedded, compute the intersection of two circles $(\tau(v_i), l_{ik}) \cap (\tau(v_j), l_{jk})$.
7:     $\tau(v_k)$ is chosen the keep the orientation of the face upward.
8:     Put the neighboring faces of $[v_i, v_j, v_k]$, which haven't been accessed yet, to the queue.
9: **end while**

5 SHAPE ANALYSIS APPLICATIONS

This section focuses on two major applications of Ricci flow in shape analysis. One is *shape indexing* and the other is *deformable surface matching*.

5.1 Shape Indexing

Surfaces can be classified by the conformal equivalence relation; two surfaces are conformally equivalent if there exists a conformal mapping between them. A conformal mapping preserves angles.

Definition 5.1 (Conformal map). *Suppose $(S_1, \mathbf{g}_1)$ and $(S_2, \mathbf{g}_2)$ are two metric surfaces, a map $\phi : S_1 \rightarrow S_2$ is* conformal *if the pull back metric induced by ϕ, $\phi^*\mathbf{g}_2$ is conformal to $\mathbf{g}_1$, $\phi^*\mathbf{g}_2 = e^{2u}\mathbf{g}_1$.*

It is unnecessary to really find the conformal mapping to verify whether two shapes are conformally equivalent. Instead, we can compute some conformal invariants for each surface, the so-called *conformal module*; if two surfaces share the same conformal module, then they
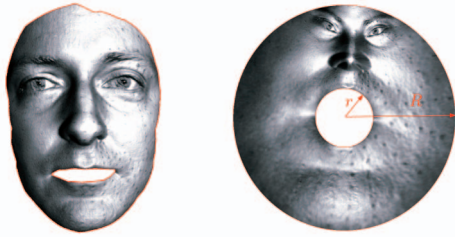
Fig. 5. A doubly connected domain is conformally mapped onto a planar annulus, and the fingerprint (conformal module) of the shape is $\frac{1}{2\pi}\log\frac{R}{r}$.

Fig. 6. A triply connected domain can be conformally mapped onto a planar disk with two circular holes using euclidean Ricci flow, and the fingerprint (conformal module) is the centers and radii of the inner circular holes. It can also be mapped onto the Poincaré disk periodically using hyperbolic Ricci flow, with all boundaries becoming geodesics. The lengths of the boundaries are the conformal module.

are conformally equivalent. The conformal module can be applied as the fingerprint of the shape.

Definition 5.2 (Teichmüller space [3]). *Given a topological surface S, the* Teichmüller space *of S is a manifold, denoted as T_S, whose points present all conformal equivalence classes of surfaces whose underlying topological structure is the same as that of S.*

In Teichmüller space, each point represents a class of surfaces, and a curve represents a deformation process from one shape to the other shape. The Teichmüller space has a Riemannian metric, which measures the angle distortion between the shapes. For genus one tori surfaces, the Teichmüller space is 2D. For genus $g > 1$ closed surfaces, the Teichmüller space is $6g - 6$-dimensional. If two surfaces share the same Teichmüller coordinates, then they are conformally equivalent. Therefore, Teichmüller coordinates can be applied to shape indexing.

In the following discussion, we focuses on genus zero surfaces with multiple boundaries. The computation of Teichmüller coordinates of general surfaces will be our future research direction.

5.1.1 Doubly Connected Domains

A genus zero surface with two boundaries is called a *doubly connected domain*, as shown in Fig. 5. The following theorem postulates that the Teichmüller space of a doubly connected domain is 1D:

Theorem 5.1 (Doubly connected domain [3]). *Suppose $(S, \mathbf{g})$ is a doubly connected domain, then it can be conformally mapped to a planar annulus, with two concentric circular boundaries. Suppose the radii of the outer boundary and inner boundary are R and r, respectively, then the conformal module of S is $\frac{1}{2\pi}\log\frac{R}{r}$.*

Therefore, the Teichmüller space of doubly connected domains is of one dimension, and the Teichmüller coordinates are given by $\frac{1}{2\pi}\log\frac{R}{r}$. Algorithm 4 computes the conformal module for a doubly connected domain.

Algorithm 4. Conformal Module for Doubly Connected Domains
Require: A triangular mesh M, which is a doubly connected domain.
1: Set target curvature equal to zero everywhere.
2: Compute a flat metric using euclidean Ricci flow Algorithm 2.
3: Compute the shortest path γ between two boundaries.
4: Slice the M along γ to get $\bar{M}$.

5: Flatten $\bar{M}$ onto the plane using euclidean embedding Algorithm 3.
6: Scale and translate the planar image of $\bar{M}$, such that the image of the outer boundary is aligned with the imaginary axis, the length of outer boundary is 2π.
7: Use the exponential map $z \to e^z$ to map the planar image of $\bar{M}$ to an annulus.
8: Measure the radii of inner and outer boundary circles r and R respectively. The conformal module is given by $\frac{1}{2\pi}\log\frac{R}{r}$.

5.1.2 Triply Connected Domains

A genus zero surface with three boundaries is a *triply connected domain*. There are two ways to represent its conformal module: One uses the euclidean metric and the other uses the hyperbolic metric. Therefore, its conformal module can be computed using either euclidean or hyperbolic Ricci flow.

Theorem 5.2 (Triply connected domain). *Suppose $(S, \mathbf{g})$ is a triply connected domain, the boundary is ordered as $\partial S = c_0 - c_1 - c_2$, where c_0 is the outer boundary and c_1 and c_2 are the two inner boundaries, then S can be conformally mapped to a unit disk with circular holes. All such mappings differ by a Möbius transformation. A canonical mapping can be obtained such that c_0 is mapped to the unit circle, the center of c_1 is the origin, and the center of c_2 is a real number. Then the centers and the radii of c_1, c_2 are the conformal module. The Teichmüller space of triply connected domains is 3D.*

Fig. 6 shows both euclidean and hyperbolic conformal modules for a triply connected domain. In Algorithm 5, we use euclidean Ricci flow to compute the canonical conformal map.

Algorithm 5. Conformal Module for Triply Connected Domain by Euclidean Ricci Flow (Generalized Koebe's Method)
Require: A triangular mesh M, which is a triply connected domain, the boundary of the mesh is $\partial M = c_0 - c_1 - c_2$.
1: **repeat**
2:     Fill c_1 by a topological disk, to get M_1.
3:     Use Algorithm 4 to map M_1 to a canonical planar annulus $\tilde{M}_1$.
4:     On $\tilde{M}_1$, remove the hole of c_1 and fill the hole c_2 to get M_2.
5:     Use Algorithm 4 to map M_2 to a canonical planar annulus $\tilde{M}_2$.

6:     On $\tilde{M}_2$, remove the hole of c_2, to get $\tilde{M}$.

7:     $M \leftarrow \tilde{M}$.

8: **until** The curvatures on the boundaries are close to constants

9: Suppose the center of c_1 is z_0, define a Möbius transformation $z \rightarrow \frac{z-z_0}{1-\bar{z}_0 z}$ to map the center of c_1 to the origin.

10: Rotate the planar image, such that the center of c_2 is on the imaginary axis.

The following theorem gives another way to define the conformal module of a triply connected domain using the hyperbolic metric:

Theorem 5.3 (Triply connected domain). *Suppose $(S, \mathbf{g})$ is a triply connected domain, the boundary is ordered as c_0, c_1, c_2. Let $\bar{\mathbf{g}}$ be the hyperbolic uniformization metric such that all of the interior points have -1 Gaussian curvature and the boundaries are geodesics (hyperbolic lines). Then the conformal module is given by the hyperbolic lengths of c_0, c_1, and c_2.*

Algorithm 6 explains the computational details for the hyperbolic conformal module.

Algorithm 6. Conformal Module for Triply Connected Domain by Hyperbolic Ricci Flow

Require: A triangular mesh M, which is a triply connected domain, the boundary of the mesh is $\partial M = c_0 - c_1 - c_2$.

1: Set the target curvature to be zero for all vertices, including boundary vertices.

2: Compute the hyperbolic metric using the hyperbolic Ricci flow Algorithm 2.

3: Find the shortest paths from c_1, c_2 to c_0.

4: Slice the mesh along the shortest paths to get $\bar{M}$.

5: Embed $\bar{M}$ onto the Poincaré disk using the Algorithm 3.

6: Measure the hyperbolic lengths of c_0, c_1 and c_2, which give us the conformal module.

The proof for the convergence of Koebe's algorithm can be found in [50]. The middle frame in Fig. 6 shows the $\mathbb{E}^2$ conformal module computed using Algorithm 5. The right frame in Fig. 6 shows the $\mathbb{H}^2$ conformal module computed using Algorithm 6.

5.1.3 Multiply Connected Domains

Genus zero surfaces with multiple holes $n > 2$ are called *multiply connected domains*. Similarly to the triply connected domain case, the surface can be conformally mapped onto a planar disk with circular holes and all such mappings differ by Möbius transformations.

Theorem 5.4 (Multiply connected domain [3]). *Suppose $(S, \mathbf{g})$ is a multiply connected domain, the boundary is ordered as*

$$\partial S = c_0 - c_1 - c_2 \cdots - c_n, n > 2,$$

where c_0 is the outer boundary. Then S can be conformally mapped to a unit disk with circular holes. A canonical mapping can be obtained such that c_0 is mapped to the unit circle, the center of c_1 is the origin, and the center of c_2 is a real number. Then the centers and radii of $c_1, c_2, \ldots, c_n$ are the conformal module. The Teichmüller space of triply connected domains is $3n - 3$-dimensional (because the center of c_1 and the x-component of c_2 are fixed).
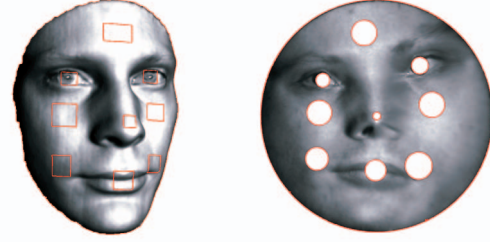

Fig. 7. A multiply connected domain is conformally mapped onto a planar disk with circular holes, and the fingerprint (conformal module) of the shape is represented as the centers and radii of the inner circular holes.

In practice, the boundary c_ks are ordered by their lengths. The computational algorithm is explained in Algorithm 7, which is very similar to that for triply connected domain.

Algorithm 7. Conformal Module for Multiply Connected Domain by Euclidean Ricci Flow (Generalized Koebe's Method)

Require: A triangular mesh M, which is a multiply connected domain, the boundary of the mesh is $\partial M = c_0 - c_1 - c_2 \cdots - c_n$.

1: **repeat**

2:     Randomly choose two circles c_i, c_j, $1 \le i < j \le n$, fill all other holes, to get $\bar{M}$.

3:     Use Algorithm 4 to map $\bar{M}$ to a canonical planar annulus $\tilde{M}$.

4:     Remove all the filled disks from $\tilde{M}$

5:     Update $M \leftarrow \tilde{M}$.

6: **until** The curvatures on the boundaries are close to constants

7: Suppose the center of c_1 is z_0, define a Möbius transformation

$$z \rightarrow \frac{z - z_0}{1 - \bar{z}_0 z}$$

to map the center of c_1 to the origin.

8: Rotate the planar image, such that the center of c_2 is on the real axis.

Fig. 7 shows the conformal module for a multiply connected domain with nine holes using Algorithm 7 based on euclidean Ricci flow.

Using hyperbolic Ricci flow, we can compute the hyperbolic uniformization metric of a multiply connected domain, but the hyperbolic lengths of all the boundaries are not enough to define the complete conformal module. For details, we refer readers to [3].

5.2 Deformable Surface Matching

Ricci flow can be applied to deformable surface matching. The approach is explained by the following commutative diagram:

$$
\begin{array}{ccc}
S_1 & \xrightarrow{\phi} & S_2 \\
\tau_1 \downarrow & & \downarrow \tau_2 \\
D_1 & \xrightarrow{\bar{\phi}} & D_2
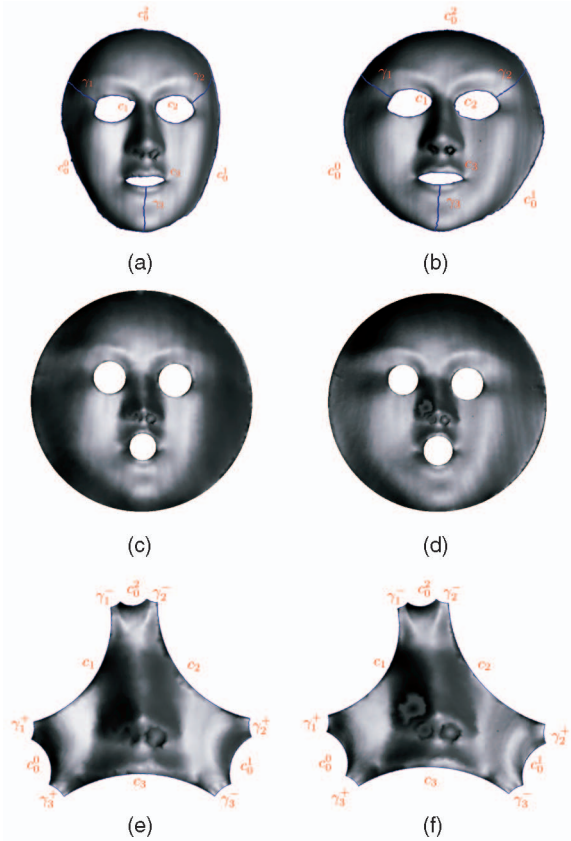\end{array}
$$

(a) (b)

(c) (d)

(e) (f)

Fig. 8. Top row: isometrically deformed surfaces. Middle row: euclidean conformal parameter domains. Bottom row: hyperbolic conformal parameter domains. The isometric mapping between the original surfaces correspond to identity maps between parameter domains from (c) to (d), and from (e) to (f). (a) Mask surface. (b) Bent surface from (a). (c) Conformal parameter domain of (a) on $\mathbb{R}^2$. (d) Conformal parameter domain of (b) on $\mathbb{R}^2$. (e) Conformal parameter domain of (a) on $\mathbb{H}^2$. (f) Conformal parameter domain of (b) on $\mathbb{H}^2$.

where S_1 and S_2 are two given surfaces and $\phi : S_1 \to S_2$ is the desired matching. We use Ricci flow to compute $\tau_i : S_i \to D_i$, which maps S_i conformally onto the canonical domain D_i. D_is are domains on the plane $\mathbb{R}^2$ or the hyperbolic disk $\mathbb{H}^2$. We call them *conformal parameter domains* of the surfaces. Then a planar mapping $\bar{\phi} : D_1 \to D_2$ is constructed using image matching techniques. The desired map ϕ is induced by $\phi = \tau_2^{-1} \circ \bar{\phi} \circ \tau_1$. This framework converts a 3D deformable surface matching problem to a 2D planar domain matching problem.

The mappings τ_1 and τ_2 are one-to-one and conformal. If $\bar{\phi}$ is a diffeomorphism, so is ϕ. If $\bar{\phi}$ is conformal, so is ϕ. As shown in Fig. 8, S_1 is a mask surface in Fig. 8a, S_2 is a deformed mask in Fig. 8b, and $\phi : S_1 \to S_2$ is the deformation between them. In our experiment, we bent S_1 to S_2 without stretching; therefore, ϕ is an isometric map. We use euclidean Ricci flow to compute $\tau_1 : S_1 \to D_1$, where D_1 is shown in Fig. 8c; $\tau_2 : S_2 \to D_2$, where D_2 is shown in frame Fig. 8d. From the figure, it is clear that Figs. 8c and 8d are identical. So, the planar map $\bar{\phi} : D_1 \to D_2$ is the identity. Therefore, ϕ is given by $\tau_2^{-1} \circ \tau_1$.

The matching based on hyperbolic Ricci flow is shown in Fig. 8. The hyperbolic conformal parameter domains are shown in Figs. 8e and 8f, where all the boundaries c_0, c_1, c_2, c_3 are mapped to hyperbolic lines. γ_k is the shortest

Fig. 9. A simply connected domain is mapped to the unit disk or the rectangle using euclidean Ricci flow.

path connecting c_0 and c_k, which is a hyperbolic line orthogonal to both c_0 and c_k. The surface is sliced along γ_k, then the conformal parameter domains become right-angled hyperbolic polygons, as shown in Figs. 8e and 8f. Similar to the method using euclidean Ricci flow, the planar map $\bar{\phi}$ is also the identity.

For the general case, our method can guarantee that the planar map $\bar{\phi}$ is a diffeomorphism; therefore, the matching ϕ is also a diffeomorphism. Our method is based on Rado's theorem.

Theorem 5.5 (Rado [51]). *Let $(S, \mathbf{g})$ be a simply connected surface, D be a convex planar domain. f is a harmonic map such that the restriction of f on the boundary $f : \partial S \to \partial D$ is a homeomorphism, then f is a diffeomorphism.*

Basically, we decompose the conformal parameter domains D_k to convex planar polygons, and construct harmonic maps between corresponding convex polygons with consistent boundary conditions. This ensures the map to be a diffeomorphism.

5.2.1 Surface Matching by Euclidean Ricci Flow

For a surface S with a simple topology, such as a simply connected domain, the conformal parameter domain D can be chosen as the unit disk, as shown in the middle frame of Fig. 9. We can also choose four points on the boundary p_0, p_1, p_2, p_3, then set the target curvature $\bar{K}(p_i) = \frac{\pi}{2}$, and zero everywhere else, the euclidean Ricci flow will conformally map the surface onto a square, as shown in the right frame of Fig. 9.

For a multiply connected domain, the conformal parameter domain is more complicated. According to Gauss-Bonnet Theorem 3.1, the total curvature is a constant. Ricci flow allows users to allocate curvatures. One approach for curvature allocation is to concentrate all the curvature on the boundaries. As shown in Fig. 8, the surface is conformally mapped to the unit disk with circular holes.
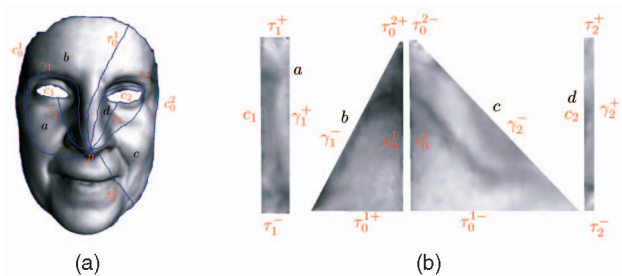

(a) (b)

Fig. 10. A triply connected domain is decomposed to convex polygons using a flat metric with cone singularity at p by euclidean Ricci flow. (a) Original surface. (b) Conformal parameter domains.

But constructing homeomorphisms between nonconvex planar domains is more difficult.

Another approach is to concentrate all the curvature on several major feature points and decompose the domain to several convex planar polygons. Fig. 10 illustrates one example. The input surface is a triply connected domain with two holes. A point p at the nose tip is chosen, such that all the curvature is concentrated at p, which is called the *cone singularity*. Then we set the target curvature at p equal to -2π, and zero everywhere else and use euclidean Ricci flow to compute the flat metric with one-cone singularity.

Under the flat metric, each boundary is a geodesic (local straight line). According to Corollary 3.2, we can compute a unique geodesic loop (local straight line) from p to itself, which is homotopic to c_k, denoted as γ_k, $k = 1, 2$. Then we compute the shortest path from p to each boundary, which is a geodesic orthogonal to the boundary. τ_1, τ_2 are the shortest paths from p to c_1 and c_2, respectively. There are two geodesics from p to c_0. The shortest loops γ_1, γ_2 and the shortest paths $\tau_1, \tau_2, \tau_0^1, \tau_0^2$ partition the surface into four segments; each segment is mapped to a planar convex polygon, as shown in Fig. 10b. Then a constrained harmonic map can be applied to match the corresponding convex polygons.

Algorithm 8 explains the details for surface matching using this approach.

Algorithm 8. Surface Matching by Euclidean Ricci Flow
Require: Two multiply-connected domains M_1 and M_2.
  1: Choose singularities $p_k \in M_k$, $k = 1, 2$.
  2: Set target curvature to be zeros for all vertices except at p_k, the target curvature at p_k is $-2\pi\chi(M_k)$.
  3: Compute the flat metric with the cone singularity using euclidean Ricci flow in Algorithm 2.
  4: Compute the shortest paths from p_k to the each boundary.
  5: For each inner boundary, compute the shortest loop (geodesic) through p_k, which is homotopic to the boundary.
  6: Decompose M_k to convex planar polygons $\{D_k^1, D_k^2 \dots D_k^n\}, k = 1, 2$.
  7: Construct the harmonic map $\bar{\phi}^j : D_1^j \rightarrow D_2^j$ with consistent boundary constraints using the method in [6].
  8: Glue the maps together to $\bar{\phi} : D_1 \rightarrow D_2$, where $D_k = \cup_j D_k^j$, $\bar{\phi}|_{D_1^j} = \bar{\phi}^j$.

The performance of the algorithm can be further improved using the following methods:

- The cone singularities are chosen at the major feature points such that the alignment of these feature points is enforced.
- We can choose multiple cone singularities on each surface. The shortest paths among these cone singularities, from singularities to the boundaries, and the shortest loops through singularities homotopic to the inner holes are used to segment the surface to convex polygons.
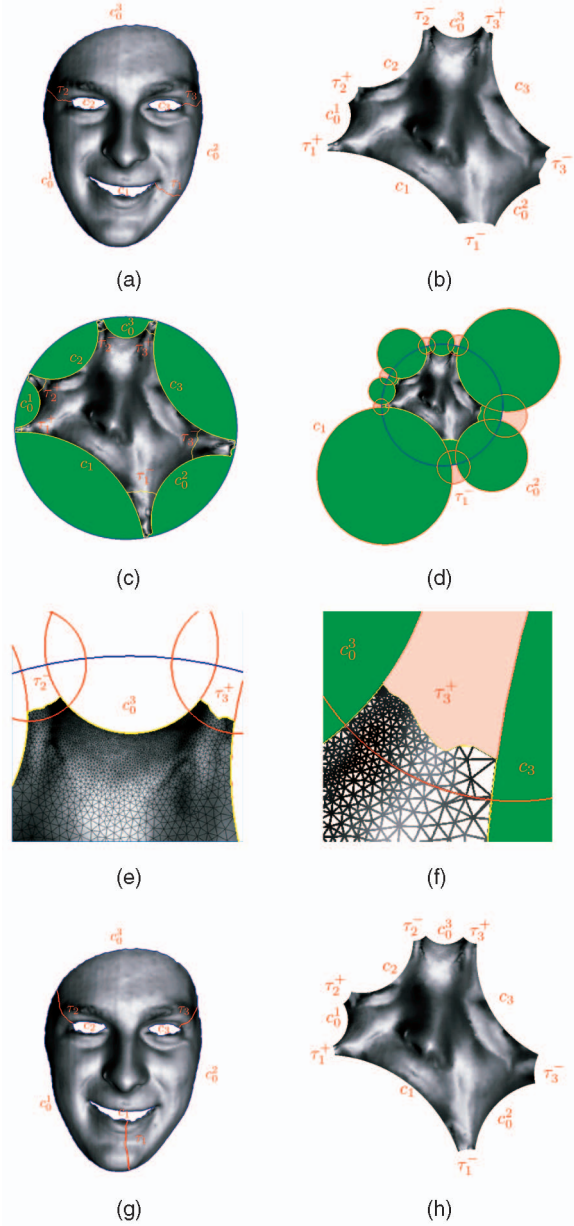- More feature point constraints can be incorporated to the local maps $\bar{\phi}^j$ from D_1^j to D_2^j.

Fig. 11. The process for computing the shortest path τ_k from boundary c_0 to boundary c_k on the Poincaré disk. (a) Shortest path in $\mathbb{E}^2$. (b) Embedding of (a). (c) Gluing copies. (d) Computing geodesics in $\mathbb{H}^2$. (e) Zoomed region. (f) Further Zoomed region. (g) Shortest path under hyperbolic metric. (h) Right-angled hyperbolic polygon.

5.2.2 Surface Matching by Hyperbolic Ricci Flow

Similarly to the matching method using euclidean Ricci flow, Algorithm 9 computes the hyperbolic metric first, then computes the shortest paths between pairs of boundaries, partitioning the surface to hyperbolic right-angled polygons (see Fig. 11). Each hyperbolic polygon in the Poincareé model is transformed to the Klein model and becomes an euclidean convex planar polygon (see Fig. 12). Harmonic maps are constructed on these convex polygons.

Algorithm 9. Surface Matching by Hyperbolic Ricci Flow
Require: Two multiply-connected domains M_1 and M_2.
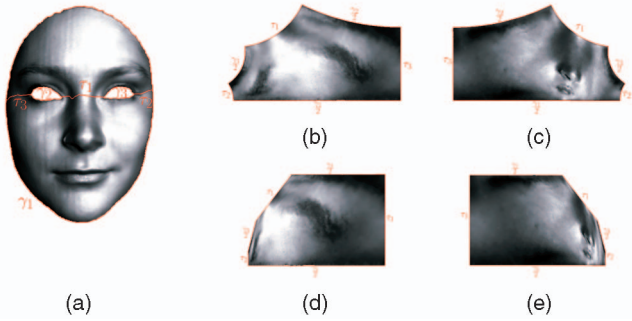 1: Compute the hyperbolic metric of M_1 and M_2 using

Fig. 12. Conversion from Poincaré hyperbolic hexagon to Klein hyperbolic hexagon, which is a euclidean convex polygon. (a) Original surface. (b) Upper Poincaré. (c) Lower Poincaré. (d) Upper Klein. (e) Lower Klein.

TABLE 1
Computational Time (s)

Name	A_0	A_1	B_0	B_1	C_0	C_1
Faces	25,783	28,212	13,671	13,461	19,414	19,120
Verts	13,162	14,374	6,983	6,865	9,908	9,759
ERF	30	30	21	20	20	20
HRF	7	7	5	4	4	4
Name	D_0	D_1	D_2	E_0	E_1	E_2
Faces	28,800	28,759	28,820	14,993	14,995	14,999
Verts	14,743	14,733	14,767	7,692	7,690	7,698
ERF	39	38	40	17	18	18
HRF	8	8	8	3	3	3

hyperbolic Ricci flow Algorithm 2, such that their boundaries become hyperbolic geodesics.

2: Compute the shortest paths under the hyperbolic metric between pairs of boundaries, which are orthogonal to the two boundaries.

3: Partition M_k consistently along the shortest paths to $\{D_k^1, D_k^2, \ldots D_k^n\}$, $k = 1, 2$, where each D_k^j is a right-angled hyperbolic polygon.

4: Construct the harmonic map $\bar{\phi}^j : D_1^j \to D_2^j$ with consistent boundary constraints.

5: Glue the maps together to $\bar{\phi} : D_1 \to D_2$, where $D_k = \cup_j D_k^j$, $\bar{\phi}|_{D_1^j} = \bar{\phi}^j$.

The second step in the algorithm is to compute the shortest path between two boundaries. This step needs more elaboration. Fig. 11 explains the details.

1. The shortest path τ_k, $k = 1, 2, 3$ from c_0 to c_k is computed using the original induced euclidean metric, as shown in Fig. 11a.

2. The surface is sliced open along $\tau_1, \tau_2,$ and τ_3. The open surface is denoted as $\bar{M}$. The open surface is flattened onto the Poincaré disk, as shown in Fig. 11b. The cutting boundaries τ_k^+ and τ_k^- are not geodesics in $\mathbb{H}^2$.

3. Compute the Möbius transformation ϕ_k such that ϕ_k maps τ_k^+ to τ_k^-, $k = 1, 2, 3$ in Fig. 11b. Suppose $\partial\tau_k^+ = p_k^+ - q_k^+$ and $\partial\tau_k^- = q_k^- - p_k^-$, then define

$$\phi_k^+ = e^{-i\theta}\frac{z - p_k^+}{1 - \bar{p}_k^+ z}, \theta = arg\frac{q_k^+ - p_k^+}{1 - \bar{p}_k^+ q_k^+},$$

where ϕ_k^+ maps p_k^+ to the origin and q_k^+ to a positive real number. Similarly, we can define ϕ_k^-, which maps p_k^- to the origin and q_k^- to a positive real number. Then the composition $\phi_k = \phi_k^- \circ \phi_k^+$ maps τ_k^+ to τ_k^-. Glue $\bar{M}$ in Fig. 11b with $\phi_k(\bar{M})$ and $\phi_k^{-1}(\bar{M})$, $k = 1, 2, 3$. The union is shown in Fig. 11c.

4. Compute the geodesics homotopic to τ_k^+ and τ_k^-. Boundary c_ks are mapped to circles. The geodesic homotopic to τ_1^- is a circle orthogonal to the unit circle (blue circle), c_1 and c_0^2, as shown in Fig. 11d. We denote the geodesics homotopic to τ_k^+ (or τ_k^-) using the same symbol τ_k^+ (or τ_k^-).

5. Figs. 11e and 11f show the zoomed region of τ_3^+. Slice the union in Fig. 11c by the geodesics τ_k^+ and τ_k^- to

get the right-angled hyperbolic polygon, as shown in Fig. 11h.

6. Map back the geodesics of τ_ks to the original surface, and slice the surface as shown in Fig. 11g.

Then we can transform the hyperbolic polygon from the Poincaré disk to the Klein model. The polygon becomes a euclidean convex polygon on the Klein disk. Fig. 12 illustrates the conversion. The mapping $\bar{\phi}$ can be computed as the harmonic map between two convex euclidean polygons, with the boundary constraints such that $\bar{\phi}$ is consistent on γ_k^+ and γ_k^-. Harmonic maps between convex planar polygons are diffeomorphisms, and this guarantees the map ϕ between two original surface to be one-to-one and onto.

In practice, there are several variations and improvements of the algorithm:

- The surface can be decomposed to several hyperbolic right-angled polygons $\{D_1^j\}$ and $\{D_2^j\}$, instead of only one polygon.
- The user can specify feature points on the boundaries. Instead of using the shortest path, the cutting curve γ_k could be the geodesic connecting the corresponding feature points on c_0 and c_k.
- Further feature constraints can be added to the harmonic maps $\bar{\phi}_j : D_1^j \to D_2^j$, either as soft constraints or hard constraints.

In general, the computation of Hyperbolic Ricci flow is more expensive than euclidean Ricci flow. Both methods enforce feature point constraints by treating them as singularities for curvature allocation purposes. However, hyperbolic Ricci flow does not require such singularities, whereas euclidean Ricci flow has to introduce them, according to the discrete Gauss-Bonnet Formula (6). Both methods map boundaries to geodesics, thus ensuring the alignment of boundary curves. For surfaces with more complex topologies, the euclidean method becomes more complex, due to the computation of the shortest paths and loops. In such cases, the hyperbolic method is more straightforward and automatic.

6 EXPERIMENTAL RESULTS

We thoroughly tested our algorithms on both 3D human face data and dynamic heart surface extracted from medical images. We captured 3D facial expression data using a phase-shifting structured light ranging system [6] at 30 frames per second.
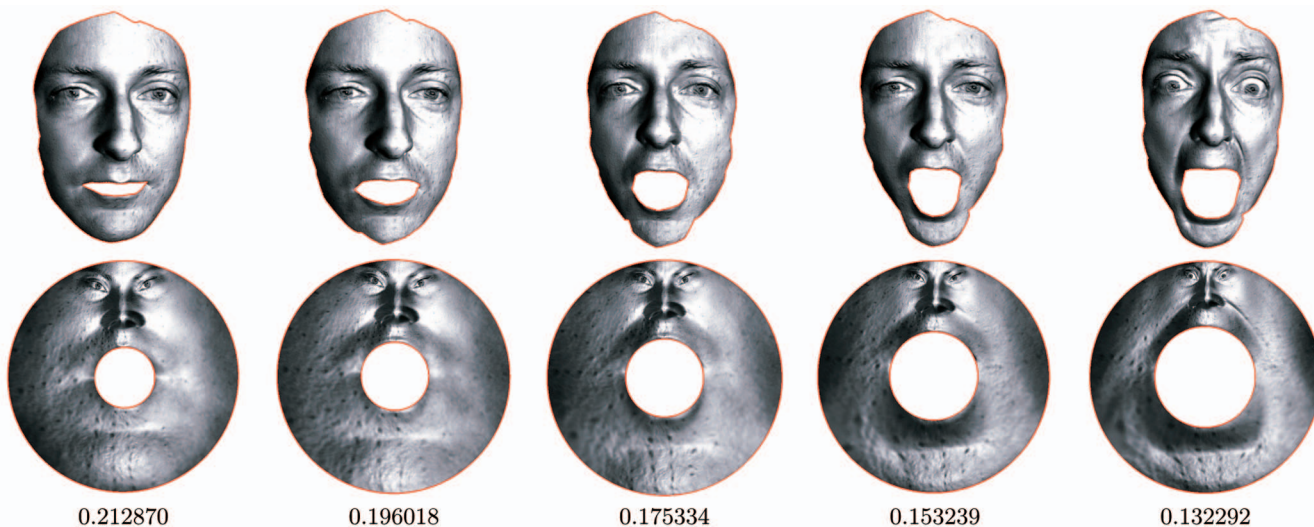
| 0.212870 | 0.196018 | 0.175334 | 0.153239 | 0.132292 |

Fig. 13. Dynamic human faces with expression changes and their conformal modules. The conformal module decreases monotonically.

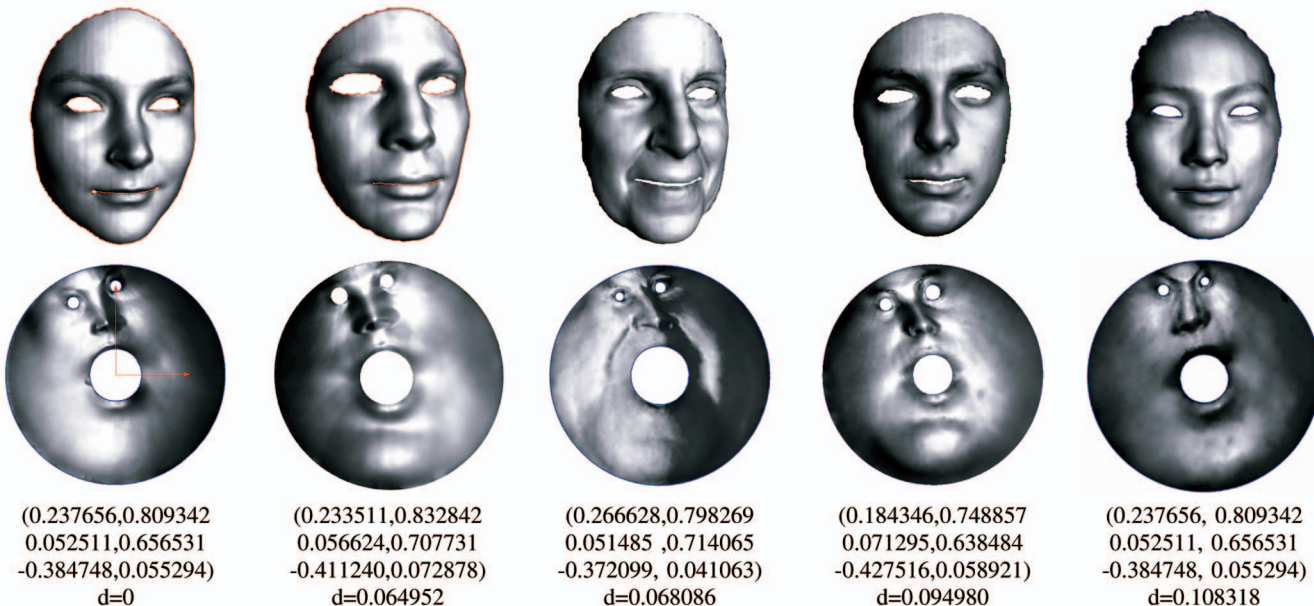| (0.237656,0.809342 0.052511,0.656531 -0.384748,0.055294) d=0 | (0.233511,0.832842 0.056624,0.707731 -0.411240,0.072878) d=0.064952 | (0.266628,0.798269 0.051485 ,0.714065 -0.372099, 0.041063) d=0.068086 | (0.184346,0.748857 0.071295,0.638484 -0.427516,0.058921) d=0.094980 | (0.237656, 0.809342 0.052511, 0.656531 -0.384748, 0.055294) d=0.108318 |

Fig. 14. Conformal modules for faces of different people with the same expression. c_1 is the mouth boundary and c_2 and c_3 are the left and right eyes. After normalization, c_1 is centered at the origin and the center of c_2 is on the positive y-axis. The conformal module is given as $(r_1, y_2, r_2, x_3, y_3, r_3)$. The distance between two surfaces is the euclidean distance between their conformal modules. The surfaces are sorted by the distance to the face on the left.

We developed our algorithms using generic C++ on windows platform. The numerical systems are solved using Matlab C++ library. The experiments are conducted on a desktop with 3.40 GHZ CPU and 3.93 GB RAM. The complexities of the testing models and the computational time are reported in Table 1 for euclidean Ricci flow (ERF) and hyperbolic Ricci flow (HRF).

6.1 Shape Indexing

6.1.1 Expression Indexing

We designed an experiment to analyze human facial expressions using Ricci flow. As shown in Fig. 13, we capture a sequence of 3D facial surfaces with an expression change. Each frame has about $265k$ faces and $133k$ vertices. In order to isolate and study the effects of expression change without ambiguities due to 3D scanning, we carefully mark the external boundaries of the face and

remove the lip boundary regions from each frame. The surface thus becomes a doubly connected domain. We use Algorithm 4 to conformally flatten the face onto the planar annuli and compute the conformal module. As we expected, as the size of the opening of the mouth increases, the conformal module decreases monotonically. This experiment indicates that the conformal module can be useful in indexing the amount of expression change.

6.1.2 Facial Geometry Indexing

We conduct another experiment to analyze human facial geometry. We capture 3D faces of different persons with the same expression. Then we extract the contour of the lips and both eyes and remove the inside regions, making the surfaces into multiply connected domains. We use Algorithm 7 to compute the conformal module of the surfaces. In details, we use euclidean Ricci flow to map

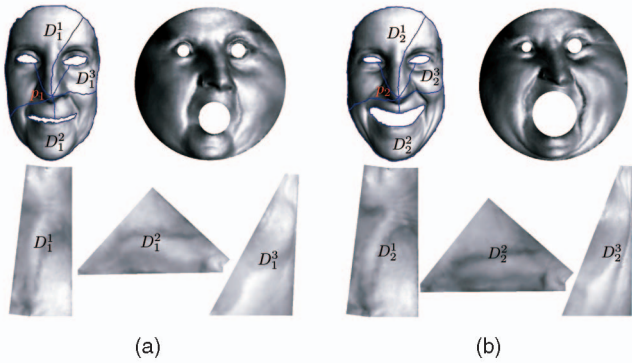(a)   (b)

Fig. 15. Matching by euclidean Ricci flow method with features. Two face scans are with large deformation. Because of the large deformation, there is a significant difference between the planar domains. Selecting the nose tip as the feature point, the surfaces are decomposed to canonical planar domains. The surfaces are registered by matching the corresponding planar domains. The registration texture error is 0.0447. (a) Calm face A_0. (b) Laughing face A_1.

the surface onto the unit disk with circular holes. Let the center of c_k is (x_k, y_k) and the radius is r_k. We use a Möbius transformation to normalize the mapping such that r_0 is 1, (x_0, y_0) is the origin, (x_1, y_1) is the origin, and x_2 is 0. Then the conformal module is given by $(r_1, y_2, r_2, x_3, y_3, r_3)$. The Teichmüller space is 6D. Fig. 14 shows the conformal modules for faces of different persons with similar expression.

6.2 Deformable Surface Matching and Registration

Ricci flow is applied to the registration of surfaces with large deformations. We evaluate the accuracy of the matching result $\phi : S_1 \to S_2$ by using the following error metrics:

$$d_g(S_1, S_2) = \frac{\int_{S_1} |\mathbf{r_1}(p) - \mathbf{r_2} \circ \phi(p)| dp}{A_1 |D(S_2)|}, \qquad (13)$$

$$d_t(S_1, S_2) = \frac{A_2 \int_{S_1} |\mathbf{t_1}(p) - \mathbf{t_2} \circ \phi(p)| dp}{A_1 \int_{S_2} \mathbf{t_2}(q) dq}, \qquad (14)$$

where d_g represents the shape error and d_t represents the texture error. $\mathbf{r_k}(p)$ represents the position vector of p on S_k. $\mathbf{t_k}(p)$ represents the texture value of p. A_k is the area of S_k. $|D(S_2)|$ is the diagonal of S_2. The shape error is formulated as the relative Hausdorff average distance (RHAD). In detail, the shape error is the average distance between the source point and the corresponding image point, normalized by the diagonal of the bounding box of the target surface. The texture error is formulated as the average texture distance between matched surfaces, normalized by the average of the texture value in the target image.

Two facial surfaces S_1, S_2 of the same person with large deformation are shown in Fig. 15, where S_1 is a neutral face and S_2 is a laughing face. The mouth and both eye regions are removed from the surface. The surfaces become a three-holed disk.

Euclidean Ricci flow method. We first use euclidean Ricci flow to map S_k to circular domains, as shown in Fig. 15. It is clear that the conformal structures of S_1 and S_2 are quite different, therefore, their conformal parameter domains exhibit significant difference. It is difficult to
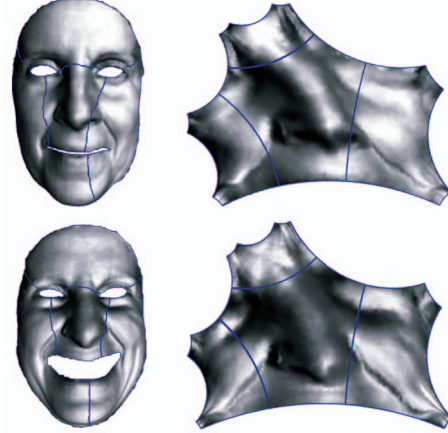

Fig. 16. Matching by the hyperbolic Ricci flow method using intrinsic domain decomposition. The shortest paths between two boundaries are computed automatically. The surfaces are decomposed by the shortest paths to right-angled hexagons. The surfaces are registered by matching the corresponding hexagons. The registration texture error is 0.0724.

construct the map between two circular domains directly. Instead we use Algorithm 8 to decompose the surface into planar polygons. We choose the nose tip as the major feature points $p_k \in S_k$. Then we set the target curvature at p_k to -4π, and zero everywhere else. We use euclidean Ricci flow to compute a flat metric with one-cone singularity p_k. Then we compute the shortest paths from p_k to all the boundaries. The shortest paths partition S_k to D_k^1, D_k^2, and D_k^3. For each pair of polygons D_1^j and D_2^j, we compute a harmonic map $\bar{\phi}^j$ with the consistent boundary constraints. Eventually, by combining all the local map $\bar{\phi}^j$s, we get the global map ϕ from S_1 to S_2.

The registration texture error between two faces in Fig. 15 is 0.0447 by the euclidean Ricci flow method. In order to demonstrate the robustness of the feature detection accuracy in our matching method, we randomly perturb the feature points around the nose tips for the two faces. The average error of three different perturbations within a 3 mm (respectively, 6 mm) radius is 0.045 (respectively, 0.048).

Hyperbolic Ricci flow method. We then register the surfaces using hyperbolic Ricci flow in Algorithm 9. We use two methods: *intrinsic domain decomposition* and *feature-based domain decomposition*.

Fig. 16 shows the intrinsic domain decomposition. S_k has four boundaries. The unique shortest paths between each pair of boundaries are computed. We slice the surface open along these shortest paths, to decompose the surface to four right-angled hyperbolic hexagons. Then we transform each hyperbolic hexagon in the Poincaré disk to a convex hexagon in the Klein model using (3). We use harmonic maps to match the corresponding hexagons and merge the local maps to one global map. The registration texture error is 0.0724.

Fig. 17 shows the feature-based domain decomposition. The user specifies feature points on the boundaries. Then the shortest paths connecting each pair of boundaries and through the corresponding feature points are computed. The surface is decomposed to hyperbolic hexagons. The maps are constructed on these hexagons. The difference
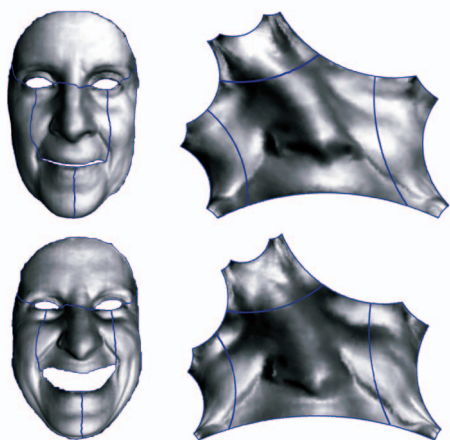
Fig. 17. Matching by the hyperbolic Ricci flow method using feature-based domain decomposition. The user specifies feature points on the boundaries; the shortest paths between two boundaries that connect corresponding feature points are computed. The surfaces are decomposed by the shortest paths to hexagons. The surfaces are registered by matching the corresponding hexagons. The registration texture error is 0.0403.
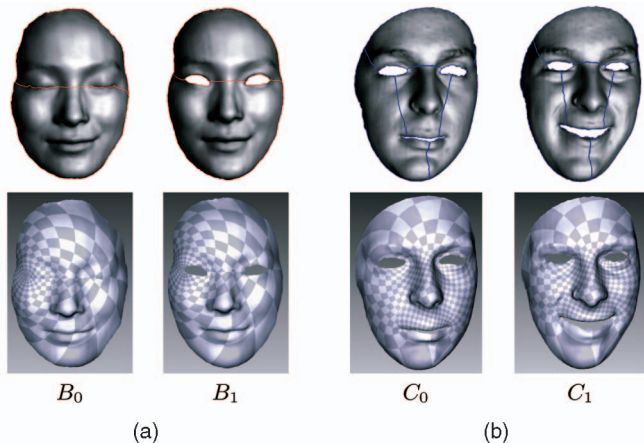

Fig. 18. Registration by the hyperbolic Ricci flow method using intrinsic domain decomposition. The registration shape errors are 1) $d_g = 0.0022$ and 2) $d_g = 0.0041$, and texture errors are 1) $d_t = 0.0813$ and 2) $d_t = 0.0731$. (a) Triply connected domain. (b) Multiply connected domain.
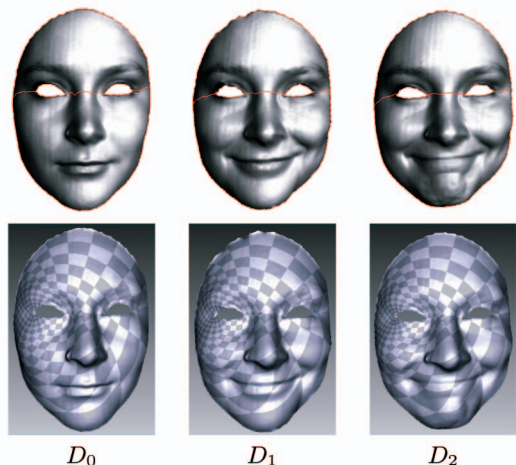

Fig. 19. Registration by the hyperbolic Ricci flow method using intrinsic domain decomposition. The registration errors between the first two faces are $d_g = 0.0025$ and $d_t = 0.0405$. The registration errors between the first and the third faces are $d_g = 0.0030$ and $d_t = 0.0411$.
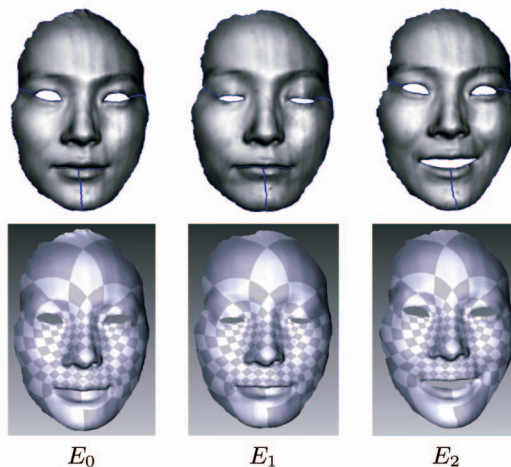

Fig. 20. Registration by the hyperbolic Ricci flow method using intrinsic domain decomposition. The registration errors between the first two faces are $d_g = 0.0042$ and $d_t = 0.0416$. The registration errors between the first and the third faces are $d_g = 0.0041$ and $d_t = 0.0416$.

TABLE 2
Registration Error under ICP, ERF, and HRF Methods

Shape(%)	B_{0-1}	C_{0-1}	D_{0-1}	D_{0-2}	E_{0-1}	E_{0-2}
ICP	2.52	2.26	2.30	2.48	3.74	2.60
HRF	0.22	0.41	0.25	0.30	0.42	0.41
Texture(%)	B_{0-1}	C_{0-1}	D_{0-1}	D_{0-2}	E_{0-1}	E_{0-2}
ERF	8.24	7.35	4.03	4.06	4.20	4.18
HRF	8.13	7.31	4.05	4.11	4.16	4.16

between intrinsic domain decomposition and feature-based domain decomposition is obvious by comparing the corresponding frames in Figs. 16 and 17. The *feature-based domain decomposition method* improves the registration texture error to 0.0403.

More experiments have been conducted for registering faces with expression changes using intrinsic domain decomposition based on Hyperbolic Ricci flow. Surfaces in Figs. 18a and 19 are with two holes, and decomposed to two right-angled hyperbolic hexagons. The matching results are illustrated using checker board texture mapping. Surfaces in Figs. 18b and 20 are with three holes.

Table 2 reports the registration error using different algorithms: Iterative Closest Point (ICP), ERF, and HRF with intrinsic domain decomposition. It can be seen that Ricci flow method achieves much better accuracy than ICP method.

6.3 Tracking Deforming Heart

In the biomedical domain, we experimented with a deforming heart sequence. The original tagged data were acquired using a 3T MRI machine. The data are image sequences from end diastole to end systole. The reconstruction was done based on methods developed by the authors of [42], who made the data available to us. The output from the analyzed data result is 3D corresponding points over time from end diastole to end systole. We experimented using a sequence of 21 frames of $3D$ corresponding points. Experiments were performed on the deforming $3D$ surface. The given $3D$ correspondences were not used in the experiments, but only as ground truth.
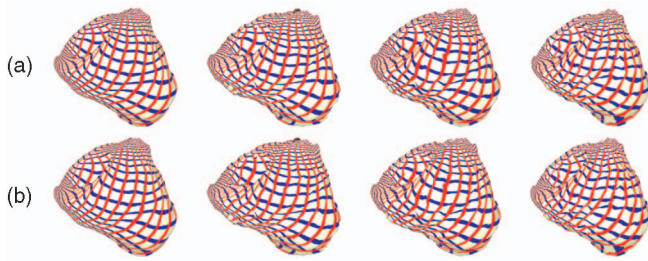
Fig. 21. Registration of 3D dynamic heart data. Registration results using euclidean Ricci flow for four different frames (1, 10, 14, 18) are shown in the top row. The original heart data for the same frames are shown in the bottom row. The data on frame 1 were texture mapped with a grid pattern, which helps to visualize the subsequent nonrigid deformations.

In order to test the robustness of our method to initial surface segmentation, we experiment using only the left ventricle data. We first detect and segment the boundary between the surface of the left ventricle and the rest of the heart. After segmenting the heart data for each frame, we apply the euclidean Ricci flow algorithm to map each heart shape into its canonical planar domain and register each adjacent frame by mapping the corresponding planar domains. In the first experiment, we manually defined a boundary on the first frame and consistently kept these points as the boundary points throughout the sequence. Even though there are large interior deformations, the boundary is sufficient in establishing almost perfect surface correspondences, with an average registration error of 0.006197. In the second experiment, the boundary was automatically determined based on curvature, using the VTK software package. These boundary points are not guaranteed to be consistent across frames. The method is still very robust with an average registration error of 0.030331.

Fig. 21 illustrates the effectiveness of registration using Ricci flow. The first frame is texture-mapped with a grid pattern both in the experimental and ground truth data, in order to better visualize the deformation. Although the nonrigid deformation of the heart is significant between different frames, our method captures the deformation almost indistinguishably from the ground truth.

7 CONCLUSION AND FUTURE WORK

This paper developed the Ricci flow method for 3D shape analysis. For shape indexing, Ricci flow is used to compute Teichmüller space coordinates for multiply connected domains. For deformable surface matching, Ricci flow is applied to map the surfaces to canonical domains, and the mapping is constructed on the 2D domains. Feature points can be incorporated to the matching process. Two computational techniques, euclidean and hyperbolic Ricci flows, were derived from the same general theoretic framework and compared.

Numerical experiments have been conducted on 3D real human face surfaces with complicated topologies and a dynamic heart sequence reconstructed from medical images. Our experimental results demonstrate that the Ricci flow method reduces the complexity of 3D geometric problems, and it is general to arbitrary surfaces, flexible for any target shapes, discriminative for shape analysis, and invariant under isometric deformations.

In the future, we will generalize shape analysis methods based on Ricci flow to high genus surfaces. We will explore Teichmüller space coordinates as compact shape signatures that can be used for object or category recognition. We will use Ricci flow for broader vision applications, such as facial expression tracking and biomedical applications.

REFERENCES

[1] G. Perelman, "Finite Extinction Time for the Solutions to the Ricci Flow on Certain Three-Manifolds," technical report, arXiv.org, July 2003.
[2] E. Sharon and D. Mumford, "2D-Shape Analysis Using Conformal Mapping," *Proc. IEEE Conf. Computer Vision and Pattern Recognition,* pp. 350-357, 2004.
[3] F.P. Gardiner and N. Lakic, *Quasiconformal Teichmuller Theory.* Am. Math. Soc., 2000.
[4] D. Zhang and M. Hebert, "Harmonic Maps and Their Applications in Surface Matching," *Proc. IEEE Conf. Computer Vision and Pattern Recognition,* pp. 524-530, 1999.
[5] Y. Wang, M. Gupta, S. Zhang, S. Wang, X. Gu, D. Samaras, and P. Huang, "High Resolution Tracking of Non-Rigid 3D Motion of Densely Sampled Data Using Harmonic Maps," *Proc. IEEE Int'l Conf. Computer Vision,* vol. 1, pp. 388-395, 2005.
[6] Y. Wang, M. Gupta, S. Zhang, S. Wang, X. Gu, D. Samaras, and P. Huang, "High Resolution Tracking of Non-Rigid Motion of Densely Sampled 3D Data Using Harmonic Maps," *Int'l J. Computer Vision,* vol. 76, no. 3, pp. 283-300, 2008.
[7] B. Levy, S. Petitjean, N. Ray, and J. Maillot, "Least Squares Conformal Maps for Automatic Texture Atlas Generation," *Proc. ACM SIGGRAPH '02,* pp. 362-371, 2002.
[8] S. Wang, Y. Wang, M. Jin, X.D. Gu, and D. Samaras, "Conformal Geometry and Its Applications on 3D Shape Matching, Recognition, and Stitching," *IEEE Trans. Pattern Analysis and Machine Intelligence,* vol. 29, no. 7, pp. 1209-1220, July 2007.
[9] M. Desbrun, M. Meyer, and P. Alliez, "Intrinsic Parameterizations of Surface Meshes," *Proc. Ann. Conf. European Assoc. for Computer Graphics,* pp. 209-218, 2002.
[10] S. Haker, S. Angenent, A. Tannenbaum, R. Kikinis, G. Sapiro, and M. Halle, "Conformal Surface Parameterization for Texture Mapping," *IEEE Trans. Visualization and Computer Graphics,* vol. 6, no. 2, pp. 181-189, Apr.-June 2000.
[11] M. Hurdal, K. Stephenson, P. Bowers, D. Sumners, and D. Rottenberg, "Coordinate Systems for Conformal Cerebellar Flat Maps," *NeuroImage,* vol. 11, p. S467, 2000.
[12] R.S. Hamilton, "The RICCI Flow on Surfaces," *Math. and General Relativity,* vol. 71, pp. 237-262, 1988.
[13] B. Chow, "The RICCI Flow on the 2-Sphere," *J. Differential Geometry,* vol. 33, no. 2, pp. 325-334, 1991.
[14] B. Chow and F. Luo, "Combinatorial RICCI Flows on Surfaces," *J. Differential Geometry,* vol. 63, no. 1, pp. 97-129, 2003.
[15] R. Campbell and P. Flynn, "A Survey of Free-Form Object Representation and Recognition Techniques," *Computer Vision and Image Understanding,* vol. 81, pp. 166-210, 2001.
[16] J. Wyngaerd, L. Gool, R. Koch, and M. Proesmans, "Invariant-Based Registration of Surface Patches," *Proc. IEEE Int'l Conf. Computer Vision,* vol. 1, pp. 301-306, 1999.

[17] S. Ruiz-Correa, L. Shapiro, and M. Meila, "A New Paradigm for Recognizing 3D Object Shapes from Range Data," *Proc. IEEE Int'l Conf. Computer Vision,* vol. 2, pp. 1126-1133, 2003.

[18] D. Huber, A. Kapuria, R. Donamukkala, and M. Hebert, "Parts-Based 3D Object Classification," *Proc. IEEE Conf. Computer Vision and Pattern Recognition,* vol. 2, pp. 82-89, 2004.

[19] B. Vemuri, A. Mitiche, and J. Aggarwal, "Curvature-Based Representation of Objects from Range Data," *Image and Vision Computing,* vol. 4, pp. 107-114, 1986.

[20] Y. Sun and M. Abidi, "Surface Matching by 3D Point's Fingerprint," *Proc. IEEE Int'l Conf. Computer Vision,* vol. 2, pp. 263-269, 2001.

[21] A. Frome, D. Huber, R. Kolluri, T. Bulow, and J. Malik, "Recognizing Objects in Range Data Using Regional Point Descriptors," *Proc. European Conf. Computer Vision,* vol. 3, pp. 224-237, 2004.

[22] T. Funkhouser, P. Min, M. Kazhdan, J. Chen, A. Halderman, D. Dobkin, and D. Jacobs, "A Search Engine for 3D Models," *ACM Trans. Graphics,* vol. 22, no. 1, pp. 83-105, 2003.

[23] R. Osada, T. Funkhouser, B. Chazelle, and D. Dobkin, "Shape Distributions," *ACM Trans. Graphics,* vol. 21, pp. 807-832, 2002.

[24] S. Wang, Y. Wang, M. Jin, X.D. Gu, and D. Samaras, "Conformal Geometry and Its Applications on 3D Shape Matching, Recognition, and Stitching," *IEEE Trans. Pattern Analysis and Machine Intelligence,* vol. 29, no. 7, pp. 1209-1220, July 2007.

[25] Y. Wang, M.-C. Chiang, and P.M. Thompson, "Mutual Information-Based 3D Surface Matching with Applications to Face Recognition and Brain Mapping," *Proc. IEEE Int'l Conf. Computer Vision,* vol. 1, pp. 527-534, 2005.

[26] D. Terzopoulos, A. Witkin, and M. Kass, "Constraints on Deformable Models: Recovering 3D Shape and Nonrigid Motion," *Artificial Intelligence,* vol. 35, pp. 91-123, 1988.

[27] X. Huang, N. Paragios, and D. Metaxas, "Establishing Local Correspondences towards Compact Representations of Anatomical Structures," *Proc. Int'l Conf. Medical Image Computing and Computer-Assisted Intervention,* vol. 2, pp. 926-934, 2003.

[28] R. Malladi, J.A. Sethian, and B.C. Vemuri, "A Fast Level Set Based Algorithm for Topology Independent Shape Modeling," *J. Math. Imaging and Vision,* vol. 6, nos. 2/3, pp. 269-290, 1996.

[29] A. Elad (elbaz) and R. Kimmel, "Bending Invariant Representations for Surfaces," *Proc. IEEE Conf. Computer Vision and Pattern Recognition,* pp. 168-174, 2001.

[30] A. Bronstein, M. Bronstein, and R. Kimmel, "Three-Dimensional Face Recognition," *Int'l J. Computer Vision,* vol. 64, no. 1, pp. 5-30, 2005.

[31] F. Memoli and G. Sapiro, "A Theoretical and Computational Framework for Isometry Invariant Recognition of Point Cloud Data," *Foundations of Computational Math.,* vol. 5, no. 3, pp. 313-347, 2005.

[32] X. Gu, Y. Wang, T.F. Chan, P.M. Thompson, and S.-T. Yau, "Genus Zero Surface Conformal Mapping and Its Application to Brain Surface Mapping," *IEEE Trans. Medical Imaging,* vol. 23, no. 7, pp. 949-958, Aug. 2004.

[33] E. Sharon and D. Mumford, "2D-Shape Analysis Using Conformal Mapping," *Proc. IEEE Conf. Computer Vision and Pattern Recognition,* vol. 2, pp. 350-357, 2004.

[34] W. Zeng, Y. Zeng, Y. Wang, X. Gu, and D. Samaras, "Non-Rigid Surface Matching and Registration Based on Holomorphic Differentials," *Proc. European Conf. Computer Vision,* 2008.

[35] S. Angenent, S. Haker, A. Tannenbaum, and R. Kikinis, "On the Laplace-Beltrami Operator and Brain Surface Flattening," *IEEE Trans. Medical Imaging,* vol. 18, no. 4, pp. 700-711, Aug. 1999.

[36] M. Jin, J. Kim, and X. Gu, "Discrete Surface RICCI Flow: Theory and Applications," *Proc. IMA Conf. Math. of Surfaces,* pp. 209-232, 2007.

[37] X. Gu, S. Wang, J. Kim, Y. Zeng, Y. Wang, H. Qin, and D. Samaras, "Ricci Flow for 3D Sahpe Analysis," *Proc. IEEE Int'l Conf. Computer Vision,* 2007.

[38] W. Zeng, X. Yin, Y. Zeng, Y. Lai, X. Gu, and D. Samaras, "3D Face Matching and Registration Based on Hyperbolic RICCI Flow," *Proc. IEEE Conf. Computer Vision and Pattern Recognition Workshop 3D Face Processing,* pp. 1-8, 2008.

[39] R. Guo, "Local Rigidity of Inversive Distance Circle Packing," arXiv:0903.1401v2, Mar. 2009.

[40] P.W. Michor and D. Mumford, "Riemannian Geometries on Spaces of Plane Curves," *J. European Math. Soc.,* vol. 8, pp. 1-48, 2004.

[41] A.C.G. Mennucci and A. Yezzi, "Metrics in the Space of Curves," 2004.

[42] W. Mio, A. Srivastava, and S. Joshi, "On Shape of Plane Elastic Curves," *Int'l J. Computational Vision,* vol. 73, no. 3, pp. 307-324, 2007.

[43] G. Charpiat, P. Maurel, J.-P. Pons, R. Keriven, and O. Faugeras, "Generalized Gradients: Priors on Minimization Flows," *Int'l J. Computational Vision,* vol. 73, no. 3, pp. 325-344, 2007.

[44] M.D. Carmo, *Differential Geometry of Curves and Surfaces.* Prentice Hall, 1976.

[45] R. Hamilton, "The RICCI Flow on Surfaces," *Math. and General Relativity,* vol. 71, pp. 237-262, 1988.

[46] G. Perelman, "The Entropy Formula for the RICCI Flow and Its Geometric Applications," technical report, arXiv.org, Nov. 2002.

[47] G. Perelman, "RICCI Flow with Surgery on Three-Manifolds," technical report, arXiv.org, Mar. 2003.

[48] M. Jin, F. Luo, and X. Gu, "Computing Surface Hyperbolic Structure and Real Projective Structure," *Proc. 2006 ACM Symp. Solid and Physical Modeling,* pp. 105-116, 2006.

[49] J. Erickson and K. Whittlesey, "Greedy Optimal Homotopy and Homology Generators," *Proc. 16th Ann. ACM-SIAM Symp. Discrete Algorithms,* pp. 1038-1046, 2005.

[50] P. Henrici, *Applied and Computational Complex Analysis,* vol. 3. Wiley Interscience, 1988.

[51] R. Schoen and S.T. Yau, *Lectures on Harmonic Maps.* Int'l Press, 1997.
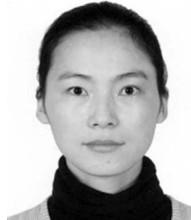
Wei Zeng received the PhD degree from the Institute of Computing Technology of the Chinese Academy of Sciences, associated with Microsoft Research Asia, in 2008. She is an assistant professor-researcher in the Department of Computer Science at Wayne State University, Detroit. She wass a research scholar in the Department of Computer Science at Stony Brook University, New York, in 2006-2009. Her research interests are computational conformal geometry and shape analysis, including surface parameterization, surface matching, registration, tracking, and recognition.

Dimitris Samaras received the PhD degree from the University of Pennsylvania in 2001. Since 2000, he has been teaching at the State University of New York at Stony Brook, where he is an associate professor and the director of the Image Analysis Laboratory. His research interests include the study of illumination in images, deformable models, face recognition, tracking and analysis of facial expression, categorical object recognition in human and computer vision, and statistical methods for the analysis of functional brain imaging data. He is a member of the IEEE.

Xianfeng David Gu received the PhD degree in computer science from Harvard University in 2003. He is an assistant professor of computer science and the director of the 3D Scanning Laboratory in the Department of Computer Science at Stony Brook University, New York. His research interests include computer vision, graphics, geometric modeling, and medical imaging. His major works include global conformal surface parameterization in graphics, tracking and analysis of facial expression in vision, manifold splines in modeling, brain mapping and virtual colonoscopy in medical imaging, and computational conformal geometry. He won the US National Science Foundation CAREER Award in 2004. He is a member of the IEEE.